Journal of Materials Science & Technology 57 (2020) 1–11

Contents lists available at ScienceDirect

Journal of Materials Science & Technology

journal homepage: www.jmst.org

Research Article

A Z-scheme heterojunction of ZnO/CDots/C_3N_4 for strengthened photoresponsive bacteria-killing and acceleration of wound healing

Yiming Xiang[a,b,c], Qilin Zhou[a], Zhaoyang Li[b], Zhenduo Cui[b], Xiangmei Liu[a,*], Yanqin Liang[b], Shengli Zhu[b], Yufeng Zheng[d], Kelvin Wai Kwok Yeung[c,*], Shuilin Wu[a,b,**]

[a] Hubei Key Laboratory of Polymer Materials, Ministry-of-Education Key Laboratory for the Green Preparation and Application of Functional Materials, School of Materials Science & Engineering, Hubei University, Wuhan 430062, China
[b] The Key Laboratory of Advanced Ceramics and Machining Technology by the Ministry of Education of China, School of Materials Science & Engineering, Tianjin University, Tianjin 300072, China
[c] Department of Orthopaedics & Traumatology, Li KaShing Faculty of Medicine, The University of Hong Kong, Pokfulam, Hong Kong, 999077, China
[d] State Key Laboratory for Turbulence and Complex System and Department of Materials Science and Engineering, College of Engineering, Peking University, Beijing 100871, China

ARTICLE INFO

Article history:
Received 5 April 2020
Received in revised form 24 April 2020
Accepted 25 April 2020
Available online 3 June 2020

Keywords:
Heterostructure
Z-scheme
Antibacterial
Wound healing
g-C_3N_4

ABSTRACT

The abuse of antibiotics is leading to the emergence of resistant bacteria. In this work, a drug-free composite of ZnO/CDots/g-C_3N_4 with Z-scheme heterojunction was developed, which was employed to kill bacteria effectively within a very short time under the irradiation of visible light due to the enhanced photocatalytic and photothermal effects. In this system, the CDots acted as a bridge between g-C_3N_4 and ZnO, effectively inhibiting the recombination of photo-generated electrons with holes and consequently enhancing the photocatalytic properties. In addition, CDots endowed the system with excellent photothermal effects. As a result, the antibacterial efficacy of ZnO/CDots/g-C_3N_4 composite against *S. aureus* and *E. coli* reached up to 99.97 % and 99.99 % respectively, after 15 min of visible light irradiation, due to the synergistic action of photo-inspired radical oxygen species and hyperthermia. The Zn ions released from the composite promoted the growth of fibroblasts, which accelerated the wound healing process.

1. Introduction

Bacterial infection is a great challenge for human health. Common bacterial infections usually exist in wounds on human body surfaces [1]. Currently, antibiotics are primarily used to fight bacterial infections. However, excessive use of antibiotics eventually results in the occurrence of drug resistance for bacteria, rendering the antibiotics ineffective [2,3]. Some traditional inorganic antibacterial agents, such as zinc oxide, copper oxide and silver, have good antibacterial properties, but the antibacterial process is uncontrollable, which may bring into an adverse effect for normal tissues [4,5]. In this light, an ideal antibacterial strategy must be one that should be antibiotics-free and has a controllable process.

In recent years, many two-dimensional semiconductor materials have been proven to have excellent photocatalytic properties to produce reactive oxygen species (ROS) under light irradiation, and the ROS can kill bacteria effectively. This method is called photodynamic therapy (PDT) [6–8]. However, traditional photocatalysts (such as ZnO and TiO_2) can only be excited by ultraviolet light, and the ultraviolet light is harmful to the human body [9,10]. On the other hand, there are many other photocatalytic materials that can be excited by near-infrared light (such as gold nanoparticles and chlorin e6) [11,12], but visible light is more readily available than near-infrared light, which is used to kill bacteria on the skin. In this regard, it is necessary to develop those composites that can be excited by visible light. Nowadays, graphitic carbon nitride (g-C_3N_4) is attracting great attention because of its adjustable band gap, band position, nontoxicity, photochemical stability, and ease of preparation [13,14]. Nevertheless, because of the quick recombination of photo-generated electrons (e^-) and holes (h^+), the photocatalytic performance of pure g-C_3N_4 is not good enough

* Corresponding authors.
** Corresponding author at: Hubei Key Laboratory of Polymer Materials, Ministry-of-Education Key Laboratory for the Green Preparation and Application of Functional Materials, School of Materials Science & Engineering, Hubei University, Wuhan, 430062, China.
E-mail addresses: liuxiangmei1978@163.com (X. Liu), wkkyeung@hku.hk (K.W.K. Yeung), shuilin.wu@gmail.com (S. Wu).

https://doi.org/10.1016/j.jmst.2020.05.016
1005-0302/

[15–17]. Thus, the current strategy is to inhibit the recombination of e^- and h^+ and further improve the overall performance of g-C_3N_4. Among these strategies, constructing g-C_3N_4 heterojunction has been found to be an effective strategy [18–20], in which the g-C_3N_4 is coupled with semiconductors with suitable band edge positions. For example, several g-C_3N_4 based composite heterojunctions, such as g-C_3N_4/CDs [21], g-C_3N_4/Ag [22], and g-C_3N_4/CdS [23], have been proved to have excellent photocatalytic effect. However, the semiconductors in g-C_3N_4-based heterojunctions must be non-toxic and can perform biological functions safely.

With consideration for these factors, in this work, we constructed a Z-scheme heterojunction composed of ZnO, g-C_3N_4 and carbon Dots (CDots) (named as ZCCN), in which, ZnO and g-C_3N_4, two common photocatalytic materials, were selected as electron carriers and acceptors, and CDots were chosen as the bridge for electrons transport to further improve photocatalytic efficiency of ZnO/g-C_3N_4 and thus enhance the yields of ROS. The CDots has no photocatalytic property of its own, but it possessed significant adsorption capabilities for h^+ and exhibited excellent electron transfer ability, facilitating ROS generation [21,24–26]. Thus, this ZCCN system effectively inhabited the recombination of e^- and h^+ and retained the strong REDOX capacity (Scheme 1), consequently producing ROS rapidly (including ·OH and $^1O_2$) under the excitation of visible light [27–29]. In addition, this system showed photothermal effects under visible light irradiation because of the photothermal property of CDots [24]. The produced ROS killed bacteria within a very short time by damaging the proteins, phospholipids, and DNA/RNA, thereby achieving a controllable rapid antibacterial efficacy [30–33]. At the same time, hyperthermia also contributed to improving antibacterial activity [34]. Furthermore, the CDots and g-C3N4 used were reported to have excellent biocompatibility [6], and the zinc ions (Zn^{2+}) released from ZnO is a necessary trace element for human body [35], the zinc ions also regulated the differentiation of wound fibroblasts (upregulating the expressions of matrix metalloproteinase-2 [MMP-2], type III collagen [COL-III], and type I collagen [COL-I]) and promoted wound healing [6,31] (Scheme 1). For comparison, g-C_3N_4 and CDots modified g-C_3N_4 were named as CN and CCN, respectively.

2. Experimental

2.1. Synthesis of CCN and ZCCN

CCN was synthesized by the thermal-polymerization of carbon dots and melamine. In a typical procedure, 2 g of melamine powder was dissolved to 10 mL of carbon dots solution (10 mg/mL). Then, the suspension was placed in a porcelain boat with a cover and subsequently heated to 500 °C for 2 h, then to 520 °C for another 2 h at the fixed heating rate of 2 °C min^{-1}. The obtained product was ground into powders using an agate mortar for further use.

Twenty milligrams of CCN powders were evenly dispersed in twenty milliliters of Dimethyl Formamide (DMF) by ultrasonication in 20 min. Zinc acetate dihydrate [Zn $(CH_3COO)_2{\cdot}2H_2O$] (0.092 *g*) was dissolved in 100 mL of DMF, and then the CCN solution was added while continually stirring in order to form a stable precursor. Subsequently, the precursor solution was maintained at 95 °C for 5 h. The color of the ZCCN powders then changed to light gray. This final product was subjected to repeated washing with ethanol and water by centrifugation. The final ZCCN powders were collected by drying the product at 55 °C.

2.2. Characterization of ZCCN

Scanning electron microscopy (JSM-6510LV, JEOL, Japan) and transmission electron microscopy (Tecnai G20, FEI, USA) were used to investigate the morphology and the microstructure of the nanomaterials. The X-ray diffraction (D8A25, Bruker, Germany) was used to analyze the phase structure of the nanomaterials. Zeta potential (Zeta; Malvern, UK) was utilized to measure the surface potential of the nanomaterials (at room temperature and pH = 7.4, the medium was phosphate-buffered saline). The X-ray photoelectron spectroscopy (Thermo Fisher Scientific 250Xi) was utilized for the elemental analysis. The photoluminescence spectra of the nanomaterials were collected by a fluorescence spectrometer. The Fourier transform infrared (JASCO FP-6500) was employed to determine the samples' functional groups. The UV–vis-NIR absorption spectra was obtained using the UV-3600 (Shimadu, Japan) between 300 nm and 800 nm. The concentrations of released zinc ions were obtained by using the inductively coupled plasma atomic emission spectrometry (ICP-AES) performed on an Optimal 8000 (PerkinElmer, USA).

2.3. Zinc ion release

In order to obtain the sustained release behavior of zinc ions, 6 mg of ZCCN was packed in dialysis bags, immersed in 30 mL PBS, and placed in an oven at 37 °C. Two mL supernatants were taken at different time points (every day for a fourteen-day period) and two mL of new PBS was added. The content of zinc ions was detected with inductively coupled plasma atomic emission spectrometry (ICP-AES).

2.4. Photothermal effect

In order to detect the sample's photothermal property, three samples (ZnO, CCN, and ZCCN) of different concentrations (100 μg/mL, 200 μg/mL) were exposed to visible light (0.6 W/cm^2). Take 1 mL of the sample solution respectively into the centrifugal tube, and use the visible light irradiate from the top. A thermal imager was applied to record temperature changes and take the thermal images. The lifting temperature curve of ZCCN was recorded at a concentration of 200 μg/mL with the Xenon lamp irradiation.

2.5. Electron spin resonance spectroscopy

The measurements of ROS were performed on electron spin resonance (ESR, JES-FA200, Japan) at room temperature. In addition, 2,2,6,6-Tetramethylpiperidine was used as a capture agent of singlet oxygen, and 5,5-dimethyl-1-pyrroline-*N*-oxide was used as a capture agent of hydroxyl radicals (·OH) during the exposure of the nanomaterials to the visible light. The production of ROS was finally analyzed by the ESR spectroscopy.

2.6. In vitro antibacterial activity test

The spread plate method was chosen to assess the antibacterial activity of the samples. Two kinds of bacteria strains, i.e., *E. coli* (Gram-negative) and *S. aureus* (Gram-positive) at a concentration of 1.0×10^7 CFU/mL were tested. Three samples (control, CCN, and ZCCN) at a concentration of 200 μg/mL were separately added into a 96-well plate with 200 μL bacteria and exposed to a Xenon lamp for 15 min. Afterwards, 10 μL of the mixed solution was diluted 100 times with Luria-Bertain (LB) media, and 20 μL of the diluted liquid was taken out and cultured on the spread agar plate for 24 h at 37 °C to get the colony number of each group. Finally, the 96-well plate was cultured at 37 °C for 24 h to investigate the long-term disinfection effect of ZCCN by Zn^{2+} release. Then, the bacterial fluids of each group were diluted 1.0×10^7 CFU/mL, and 20 μL of the diluted fluid was taken out to the spread agar plate and evenly distributed. These plates were then cultured at 37 °C for 24 h. The

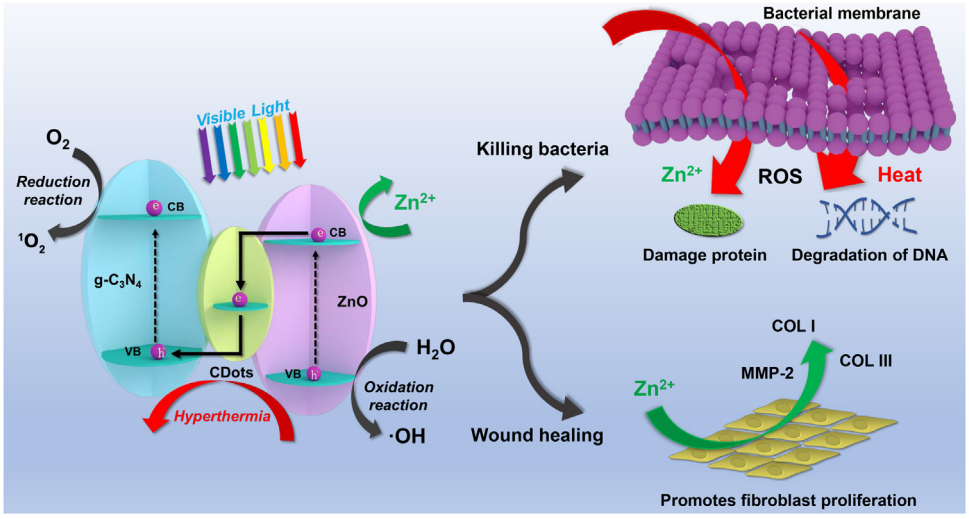

Scheme 1. Schematic illustration of the Z-scheme ZnO/CDots/g-C_3N_4 composite for photoresponsivity bacteria-killing and acceleration of wound healing.

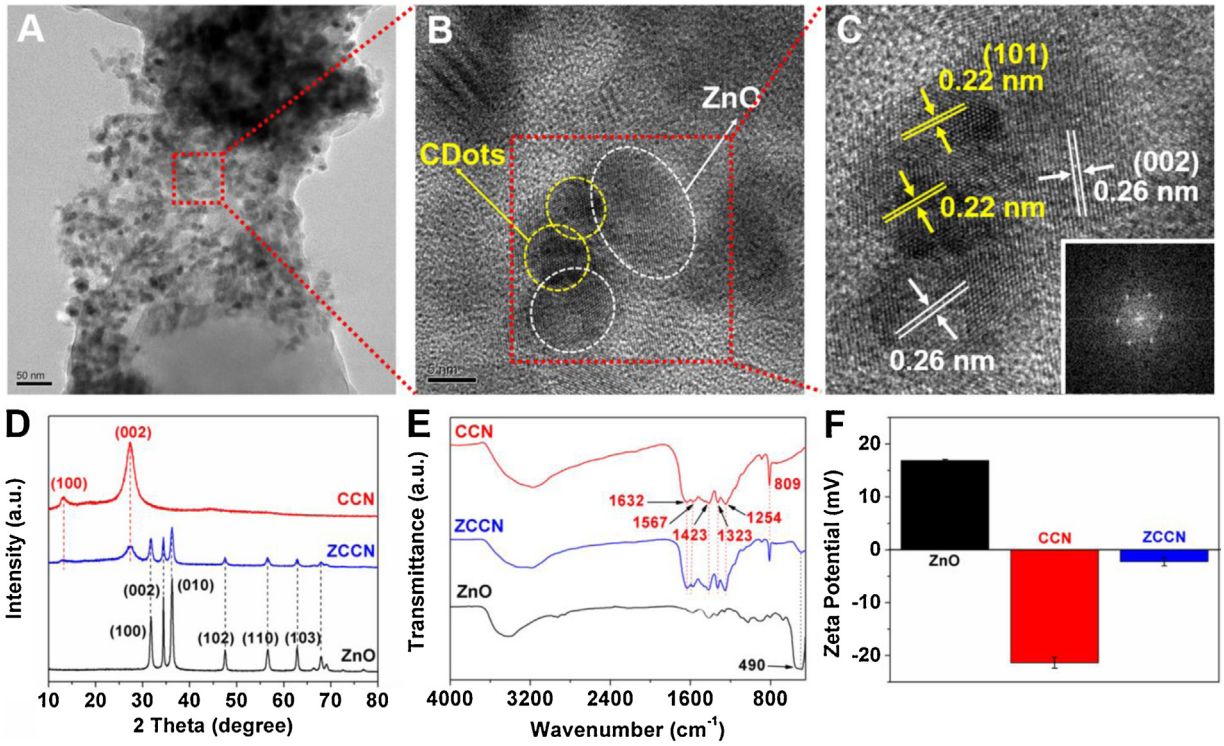

Fig. 1. (A) TEM image of the ZCCN. (B) Magnified TEM image of the ZCCN. (C) HRTEM image of CDots and ZnO embedded in g-C_3N_4 and corresponding FFT pattern of the CDots. (D) XRD patterns of the CCN, ZCCN and ZnO. (E) FT-IR spectra of the CCN, ZCCN and ZnO. (F) Surface ζ-potential of the CCN, ZCCN and ZnO.

long-term disinfection effect of ZCCN was also indicated by the optical density of 100 μL bacteria fluid at 600 nm. The disinfection ratio of samples was calculated by the following equation: disinfection ratio (%) = (number of CFUs in control group - number of CFUs in experimental group) / (number of CFUs in control group) × 100 %.

2.7. In vitro cytotoxicity assay and quantitative real-time polymerase chain reaction

NIH3T3 cells were cultured in a medium supplemented with 10 % fetal bovine serum and 1% penicillin-streptomycin solution (HyClone) in a humidified atmosphere of 5% CO_2 at 37 °C, and the medium was changed every 2 days. The cytotoxicity test was performed by an indirect contact method. The cells were seeded into 96-well plates. After culturing for 1 day, the samples were added in the 96-well plates and then continued to culture for 1, 3, and 7 days in the incubator. The medium as the positive control and a medium including 10 % dimethyl sulfoxide as the negative control. Then, 10 mL of cell counting kit (CCK-8) solution was added to each well. The cells were incubated with CCK-8 for 3 h. Then, the absorbance of each well was tested by SpectraMax i3 Platform (Molecular Devices, California, USA) at the wavelength of 450 nm. Viability of cells (X) was calculated using the following formula according to ISO 19003−5: $X = (OD_1/OD_2) \times 100$ %. Here, OD_1 was the mean absorbance of the experimental sample groups and neg-

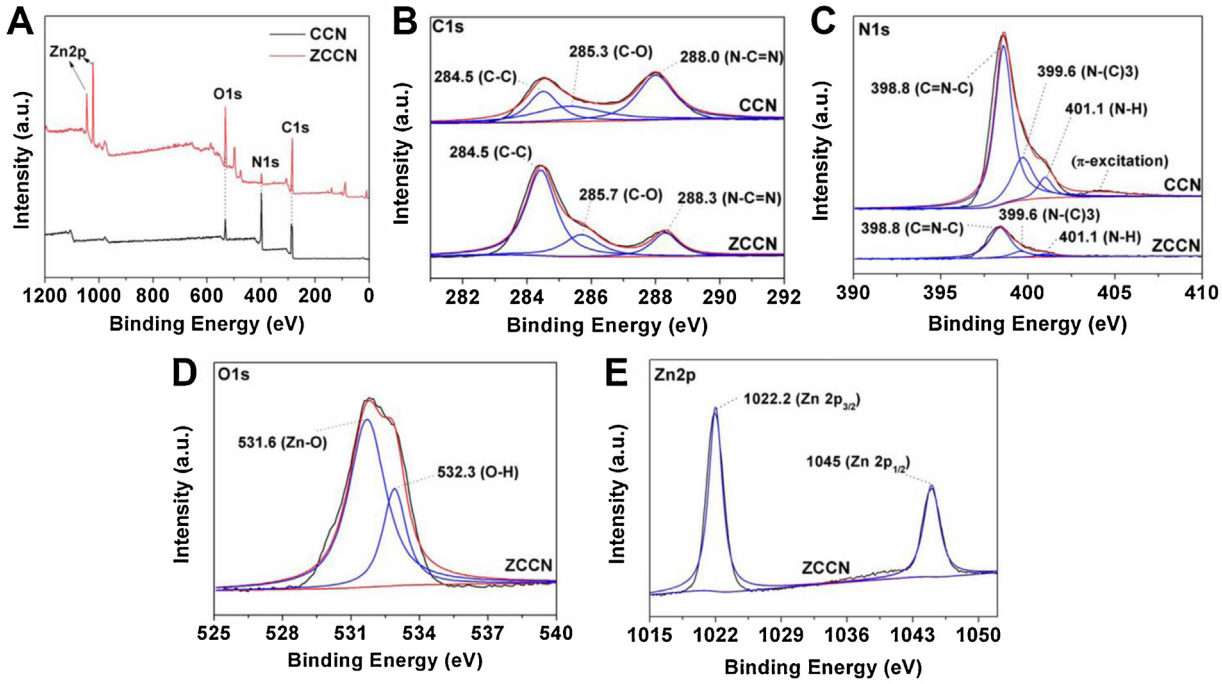

Fig. 2. (A) XPS survey scan of the CCN and ZCCN. XPS high-resolution spectra of (B) C 1s peaks and (C) N 1s peaks obtained from CCN and ZCCN. XPS high-resolution spectra of (D) O 1s peaks and (E) Zn 2p peaks obtained from ZCCN.

ative control group; OD_2 was the mean absorbance of the positive control group.

The expression of genes (MMP-2, COL-III, and COL-I) related to tissue repair was analyzed by a quantitative real-time polymerase chain reaction (qRT-PCR). NIH3T3 cells were seeded with samples or PBS (control group) in 6-well plates and cultured with 2 mL of culture medium (refreshed every 2 days). The details of the qRT-PCR were as follows: the culture medium was removed from each well, and the cells were washed with cold PBS twice at 2 days and 5 days. Afterward, following the manufacturer's guidelines, the RNA was extracted by a total RNA kit I (50) (OMEGA R6834−01). The quantification and reverse transcription of all RNA were conducted with a Nanodrop 2000 spectrophotometer (Thermo Scientific) and PrimeScript RT Master Mix (Perfect Real Time) (Takara). A qRT-PCR was performed on a BIO-RAD system using SYBR Green Master Mix. The quantitative qRT-PCR results were analyzed by ΔCt calculation; the primer sequences were listed in Table S1 (in Supporting Information).

2.8. In vivo animal experiments

The *in vivo* animal experiments were approved by Hubei Provincial Centers for Disease Prevention & Control, and the male Wistar rats (180−220 g body weight) were bought from Wuhan Centers for Disease Prevention & Control. Before the test, the rats were individually raised in cages for two days and eventually divided into two groups (treatment and control groups). The simulated skin wounds were created on the back of the rats and injected with 20 μL 1×10^8 CFU mL^{-1} *S. aureus*. The wounds of two groups were treated with 10 μL 100 μg/mL ZCCN or the PBS solution (control group). Then, the wounds of two groups were exposed to the visible light for 10 min and patched with medical gauze. After 2, 6, and 12 days, the wounds were observed and photographed. The wound tissues were extracted and fixed with 10 % formalin and then stained and photographed. Blood was collected from the rats for routine analysis on a veterinary automatic blood cell analyzer (Mindray BC-2800 Vet). The major organs (heart, liver, spleen, lungs, and kidney) were evis-cerated and stained with H&E and examined by digital microscopy after 12 days.

2.9. Statistical analysis

All experiment data were evaluated as means ± standard deviations based on, at a minimum, three tests and contrasted via Kruskal-Wallis one-way analysis of variance (ANOVA).

3. Results and discussion

3.1. Characterization of ZCCN

Transmission electron microscopy (TEM) image showed that the prepared composites of ZCCN comprised numerous nanoparticles (Fig. 1(A)), and the high-resolution TEM image revealed that these nanoparticles were composed of CDots (~5 nm in diameter) and ZnO nano particles (5−10 nm) embedded in a g-C_3N_4 (Fig. 1(B)). The enlarged view of the high resolution TEM (HRTEM) image showed an interplanar spacing of 0.22 nm in the crystalline CDots (Fig. 1(C)), which corresponds to the (101) spacing of graphitic carbon [21]. The HRTEM image of ZnO showed the interplanar spacing of 0.26 nm corresponding to the (002) spacing of ZnO (Fig. 1(C)) [20]. The 2D fast Fourier transform pattern was showed in Fig. 1(C), and the hexagonal crystalline structure proved the existence of CDots evidently [21]. Fig. S1 (in Supporting Information) displayed the surface morphologies and the corresponding energy dispersive spectroscopy (EDS) mapping of C, N, O, and Zn for the prepared CCN and ZCCN. Obviously, C, N, and O were homogeneously distributed in the CCN and ZCCN. There were no signal of Zn in CCN while after the addition of ZnO, however, the composite of ZCCN exhibited strong Zn signal with homogeneous distribution.

X-ray diffraction (XRD) patterns were performed to investigate the phase structure of the ZCCN system. As shown in Fig. S2 (in Supporting Information), the g-C_3N_4 atomic structure did not change significantly with the addition of CDots [24]. In the XRD pattern obtained from CCN (Fig. 1(D)), the sharp diffraction peak (002) at

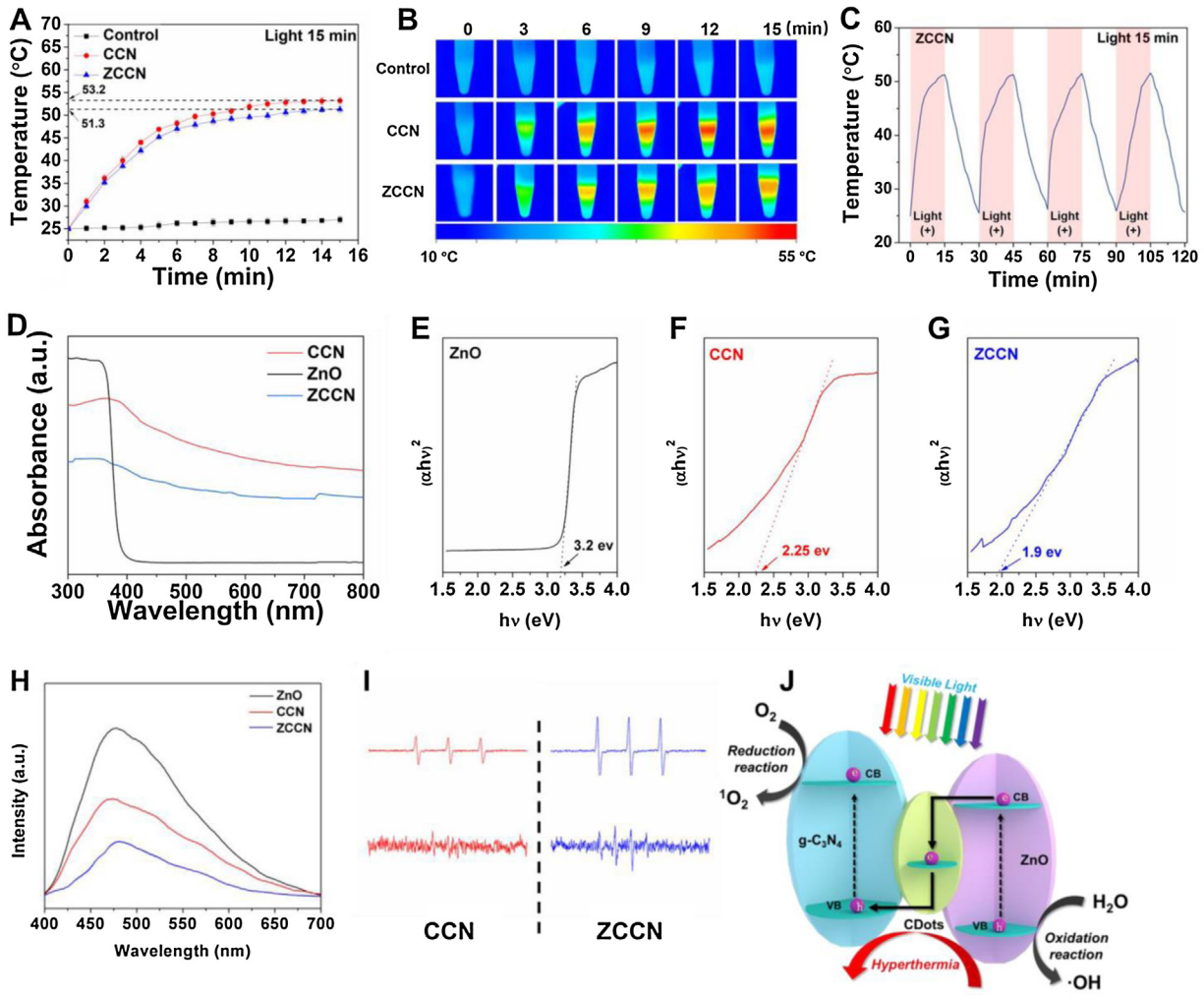

Fig. 3. Photoresponsivity properties of different groups. (A) Photothermal curves under 15 min visible light irradiation. (B) Real-time infrared thermal images of different samples under visible light irradiation for 15 min. (C) Temperature rising and cooling of the ZCCN when the irradiation is on/off. (D) UV–vis results of the CCN, ZCCN and ZnO. Bandgap calculated from UV–vis spectra of (E) ZnO, (F) CCN and (G) ZCCN. (H) PL spectra investigated with 325 nm excitation wavelength of ZnO, CN and ZCCN from 400 to 700 nm. (I) ESR spectra of ZCCN after visible light irradiation for 15 min. (J) Illustration of photoresponsivity performance process in ZCCN under visible light.

27.4° indicated an interlayer aromatic structure, while the weaker (001) diffraction peak at 13.8° was ascribed to the planar structure [36–38]. The XRD pattern of ZnO showed the most stable form of a wurtzite hexagonal ZnO phase. The existence of ZnO on the CCN was confirmed by the ZnO characteristic diffraction peaks (100), (002), (101), (102), (110) and (103) appearing in the ZCCN pattern, and all the positions of these peaks were in keeping with the standard ZnO bulk (JCPDS no. 36-1451) [20,31,39].

Fourier transform infrared (FT-IR) spectra were examined to further explore the compositions of the samples. As shown in Fig. 1(E), in the CCN curve, the peak at 809 cm^{-1} was ascribed to the triazine units and the peaks at 1254, 1323, and 1423 cm^{-1} were assigned to the aromatic C—N [36]. The C—N stretching vibration modes were proved by the peaks located at 1567 and 1632 cm^{-1} [40]. These characteristic peaks also appeared in the ZCCN curve. In addition, the representative peak (Zn-O bending vibrations) of ZnO at 490 cm^{-1} was also observed in the ZCCN curve [29,31]. These FT-IR results and the XRD results confirmed the successful synthesis of ZnO/CDots/g-C_3N_4 together. In Fig. 1(F), the ζ-potential measurements also proved that the ZnO successfully was loaded on the surface of the CCN. The surface potential of positively ZnO decreased from 17.4 to -3.1 mV after CCN (-22.3 mV) combination.

The XPS survey spectra of CCN and ZCCN were shown in Fig. 2(A). The comparison of the two curves illustrated that after the addition of ZnO, a significant Zn 2p peak appeared in ZCCN, while the peak of O 1s was strengthened and the peak of N 1s was weakened. The C 1s spectrum of CCN presented in Fig. 2(B) showed three peaks at 284.5 eV, 285.3 eV, and 288.0 eV. The C peak at 288.0 eV was identified as sp^2-bonded carbon (N—C═N) of g-C_3N_4; the peak at 285.3 eV was attributed to adventitious carbon due to the possible contamination in air during fabrication; and the weaker one at 284.5 eV corresponded to graphitic carbon (C—C) [20,41,42]. Similar peaks of C 1s, which shifted to a higher direction, were also observed in ZCCN.

As shown in Fig. 2(C), the N 1s spectrum of CCN at 398.8 eV corresponded to sp^2-bonded nitrogen (C = N—C). The peak at 399.6 eV was assigned to the N-(C)3 groups, and the peak centered at 401.1 eV corresponded to the N—H groups. Moreover, the weak shoulder peak at 403.2 eV accounted for π-excitations [21]. These three peaks of N 1s also existed in ZCCN. The O 1s peak at 531.6 eV belonged to the Zn-O and the other one at 532.3 eV belonged to the O—H adsorbed on the surface (Fig. 2(D)) [20]. For the Zn 2p spectrum (Fig. 2(E)), the peaks at 1022.2 and 1045.0 eV in ZCCN were attributed to Zn $2p_{3/2}$ and Zn $2p_{1/2}$ [43].

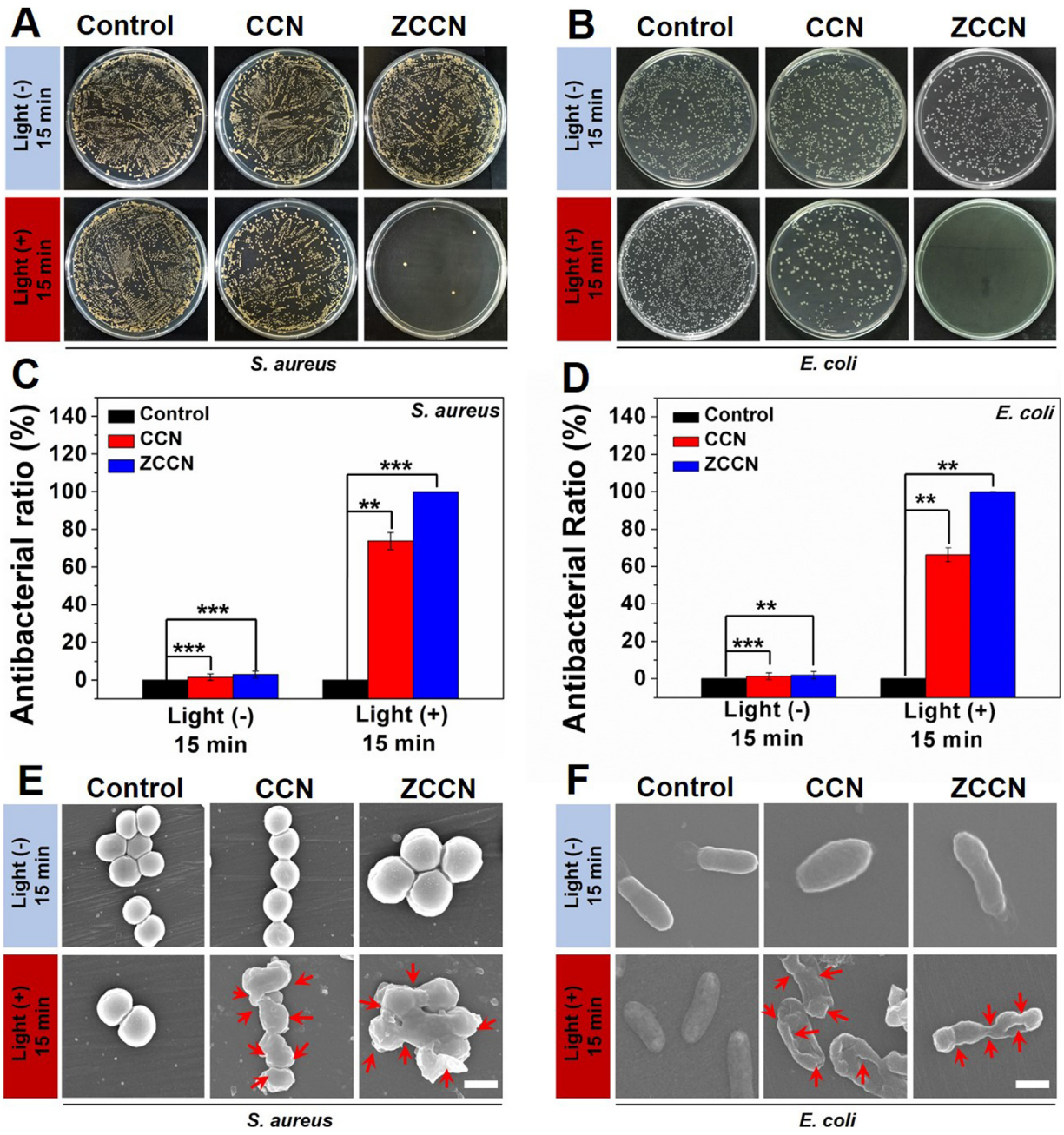

Fig. 4. Spread plate results of (A) *S. aureus* and (B) *E. coli* grown on different samples; Antibacterial activity of different samples against (C) *S. aureus* and (D) *E. coli*; Surface morphologies of (E) *S. aureus,* and (F) *E. coli* treated with different groups with or without 15 min visible light irradiation, scale bars: 1 μm. Error bars indicate means ± standard deviations: $^{**}p < 0.01$, and $^{***}p < 0.001$.

These results indicated that ZnO and CCN were combined successfully.

3.2. Photothermal and photodynamic effects

The photothermal effect of CCN and ZCCN under visible light irradiation was measured by several different tests. The temperature change was measured by the photothermal imager (Fig. 3), with phosphate buffer solution (PBS) as the control group. After visible light irradiation for 15 min, the temperature of both CCN and ZCCN increased by more than 50 °C due to the CDots that were triggered to produce heat. In Fig. 3(A), the final temperature of the CCN reached up to 53.2 °C, while the ZCCN only got to 51.3 °C. The little decrease was ascribed to the covering of ZnO on CDots in the latter, weakening the light absorption and the ZnO had no photothermal effect of its own. Fig. 3(B) showed IR thermal images obtained from the groups of PBS, CCN and ZCCN under 15 min visible light irradiation. As illustrated, the PBS group showed minimal changes while both CCN and ZCCN exhibited obvious increase of temperature as the irradiation time increased, which was consistent with the photothermal curves shown in Fig. 3(A). Furthermore, the temperature of the ZCCN exhibited a stable effect even after light irradiation for four cycles (Fig. 3(C)). These results proved that visible light was absorbed by the prepared composite and converted into heat. As a result, the excellent photothermal properties of ZCCN were demonstrated.

Fig. 3(D) showed the UV–vis results of all the samples. ZnO displayed its intrinsic absorption only at 390 nm [44]. Compared with

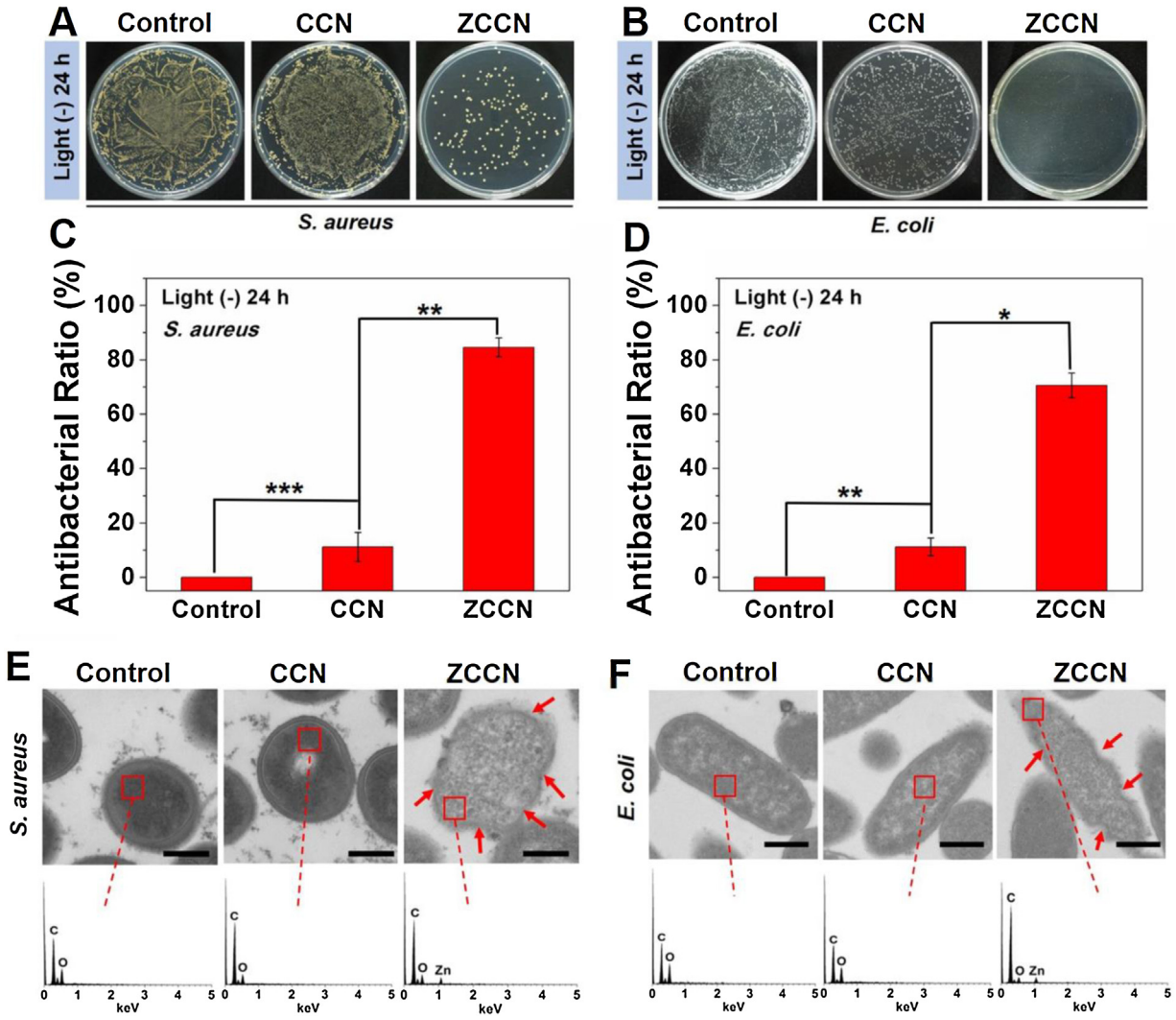

Fig. 5. Spread plate results of (A) *S. aureus* and (B) *E. coli* grown on different samples without light irradiation for 24 h. Antibacterial ratio of different samples against (C) *S. aureus* and (D) *E. coli* via agar plating method. TEM images and corresponding EDS analysis of intracellular sections of (E) *S. aureus* and (F) *E. coli* cultured with different samples. Scale bars are 200 nm. Error bars indicate means ± standard deviations: $^{*}p < 0.05$, $^{**}p < 0.01$ and $^{***}p < 0.001$.

ZnO, the CCN and ZCCN sample exhibited stronger light absorption in the whole light regions. The increased absorption of light was attributed to the CDots in the sample. Moreover, the light absorption of ZCCN was slightly less than that of CCN due to the presence of ZnO, but that didn't affect light absorption of ZCCN in both ultraviolet and visible light regions [38]. As shown in Fig. 3(E)-(G), the bandgap of different groups was calculated by the following equation:$(\alpha hv)^n = C(hv - E_g)$. The bandgap of pure ZnO was 3.2 eV and the bandgap of the CCN was 2.25 eV. After the combination of ZnO and CCN, the bandgap of ZCCN (1.9 eV) was obviously reduced compared to CCN, these results reveal that the ZCCN was a more efficient visible light photocatalyst.

In Fig. 3(H), the photoluminescence (PL) emission intensities of ZnO, CCN and ZCCN were compared to understand the interfacial charge transfer and separation efficiency of photogenerated electron-hole pairs. After the ZnO was added, the peaks of ZCCN were decreased compared to those of CCN, indicating the enhanced transport of photo-generated electrons and thus reducing the recombination of electron-hole pairs.

Fig. 3(I) showed the ESR spectra obtained from different samples. To detect singlet oxygen ($^1O_2$), 2,2,6,6-Tetramethylpiperidine (TEMP) was used. The typical ESR spectra were only observed in ZCCN groups under 15 min visible light irradiation. The three peaks were the characteristic peaks of the reaction products between TEMP and $^1O_2$ [45], indicating that the singlet oxygen was only produced from ZCCN. Except the singlet oxygen, hydroxyl radical (·OH) is the other part of ROS. To investigate the effects of the ZCCN on generation of ·OH, 5,5-dimethyl-1-pyrroline-*N*-oxide (DMPO) was selected. Four peaks were observed in the ESR spectrum of ZCCN, while the CCN had almost negligible peaks. The four peaks were the characteristic peaks of the reaction products between DMPO and ·OH. Obviously, the ESR signals of ZCCN were more obviously than those of (Fig. 3(I)) and the control group (Fig. S3 in Supporting Information). Consequently, the yield of ROS in the latter was higher than that in the former. This result was consistent with the results obtained by PL spectra (Fig. 3(H)).

Fig. 3(J) showed the photocatalytic mechanism (Z-scheme electron transfer) of ZCCN. Under visible light irradiation, both g-C_3N_4 and ZnO could generated electron-hole pairs. The excited e^- from ZnO were transferred (by CDots) to combine with the photogenerated h^+ in g-C_3N_4, so that the electrons with stronger reducibility in conduction band (CB) of g-C_3N_4 and holes with stronger oxidization ability in valence band (VB) of ZnO could be remained. Finally, the electrons from CB of g-C_3N_4 reacted with surrounding O_2 to produce $^1O_2$, and meantime, the photogenerated holes in ZnO reacted

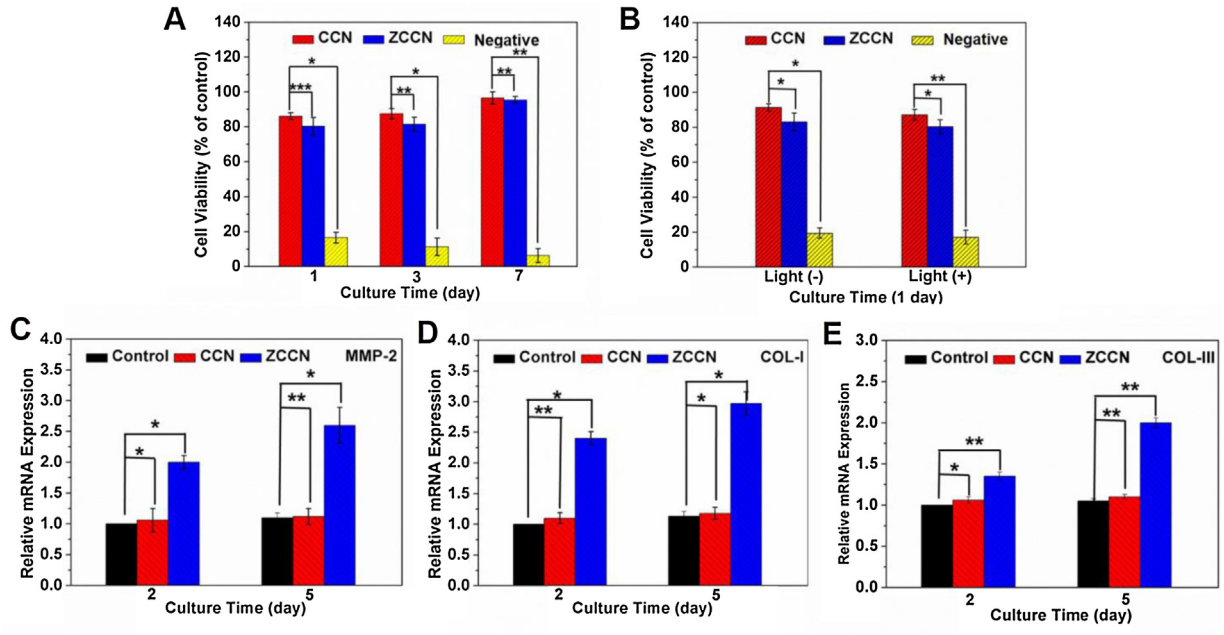

Fig. 6. (A) Cell viability of NIH3T3 treated with all samples at day 1, 3, and 7. (B) Cell viability of NIH3T3 treated with all samples after 15 min mixed light irradiation at day 1. Gene expression measured by qRT-PCR of the angiogenic genes (C) MMP-2, (D) COL I, and (E) COL III for fibroblasts incubated for 2 and 5 days in media containing different samples. The error bars indicate means ± standard deviations: $^{*}p < 0.05$, $^{**}p < 0.01$, and $^{***}p < 0.001$.

with H_2O to produce $^{\bullet}OH$. At the same time, the CDots produced heat under visible light.

3.3. *In vitro antibacterial ability*

Visible light was selected for antibacterial experiments. The antibacterial activities of all samples (with PBS control group) against Gram-positive bacteria (*S. aureus*) and Gram-negative bacteria (*E. coli*) were conducted by spread plate method. The antibacterial ratio was calculated by counting the number of bacterial colony-forming units (CFUs) (Fig. 4). As shown in Fig. 4(A) and (B), it was obviously that only visible light irradiation did not affect the growth of bacteria as the bacteria number in the control group almost showed no change. On the other hand, there was no obviously reduction of *S. aureus* and *E. coli* in the CCN and ZCCN compared to the control group without visible light irradiation, indicating that both CCN and ZCCN had no antibacterial activity without light in a short time. In contrast, the ZCCN group exhibited a minimum of bacteria than any other groups under 15 min visible light, and the calculated antibacterial ratio of ZCCN against *S. aureus* and *E. coli* were 99.97 % (Fig. 4(C)) and 99.99 % (Fig. 4(D)), respectively, which was ascribed to the synergistic effects of highly efficient photodynamic and photothermal properties of the prepared ZCCN under visible light irradiation (shown in Fig. 3). There was an interesting phenomenon, the number of bacteria also decreased in the CCN group under visible light, and the antibacterial ratio against two kinds of bacteria were approximately 72.8 % and 69.2 % (Fig. 4(C) and (D)), ascribing to the local hyperthermia and a very small amount of ROS produced by CCN under visible light. The morphologies of bacteria in different samples were examined by SEM (Fig. 4(E) and (F)). Those bacteria from the control group showed integrated membranes and regular shapes regardless of irradiation or not. The same normal structures were observed in the bacteria from the CCN and ZCCN groups without irradiation, indicating little antibacterial activity of all groups in the darkness within a short culturing time, which was in good agreement with spread plate results. When irradiated by visible light, the normal structures of bacteria were disrupted, i.e., the bacterial membrane was shrunken and even broken (marked by red arrows).

As shown in Fig. 5(A) and (B), after culturing without light irradiation for 24 h, both CCN and ZCCN groups exhibited lower antibacterial efficacy than the corresponding groups with 15 min light irradiation in Fig. 4(A) and (B). The antibacterial ratio of CCN towards *S. aureus* and *E. coli* were approximately 15.2 % and 14.8 %, respectively, while the antibacterial ratio of ZCCN against *S. aureus* and *E. coli* were approximately 82.9 % and 68.7 %, respectively (Fig. 5(C) and (D)). Obviously, since little hyperthermia or ROS was produced without light, the observed antibacterial activity was ascribed to the released Zn^{2+} from ZCCN, which has been reported to inhibit bacterial activity [46,47]. The ZCCN groups exhibited gradual leaching of Zn^{2+} during immersion in PBS for 14 days (Fig. S4 in Supporting Information).

The TEM and EDS analysis were used to investigate whether the Zn^{2+} intruded into the bacteria. In the control groups and CCN groups, the TEM images showed intact cell walls and the EDS analysis showed that there was no Zn in the bacteria (Fig. 5(E) and (F)). By contrast, in the ZCCN groups, obvious distortion was observed, and EDS analysis showed the existence of Zn in the broken bacteria (red rectangles). It has been reported that Zn^{2+} can enhance oxidative stress and combine with the bacteria to change the fluidity of the bacterial membrane, thus killing the bacteria [5,46].

3.4. *In vitro cytotoxicity studies and cell response*

NIH3T3 (mouse embryonic fibroblast cell line) were used to evaluate the cytotoxicity of the prepared CCN and ZCCN. Fig. 6(A) illustrated cell viabilities of NIH3T3 cultured in the negative control (a medium including 10 % dimethyl sulfoxide) and other groups after culturing for 1, 3, and 7 days. The cell viability of all groups did not show significant changes at the 1-day and 3-day stages; at 1-day stage, the cell viability of the CCN was 86.2 %, and the cell viability of the ZCCN was 79.1 %. The cell viability of the CCN gradually increased from 86.2 % at 1 day to 98.3 % at 7 days. The cell viability also increased for the ZCCN group from 79.1%–97.1% at

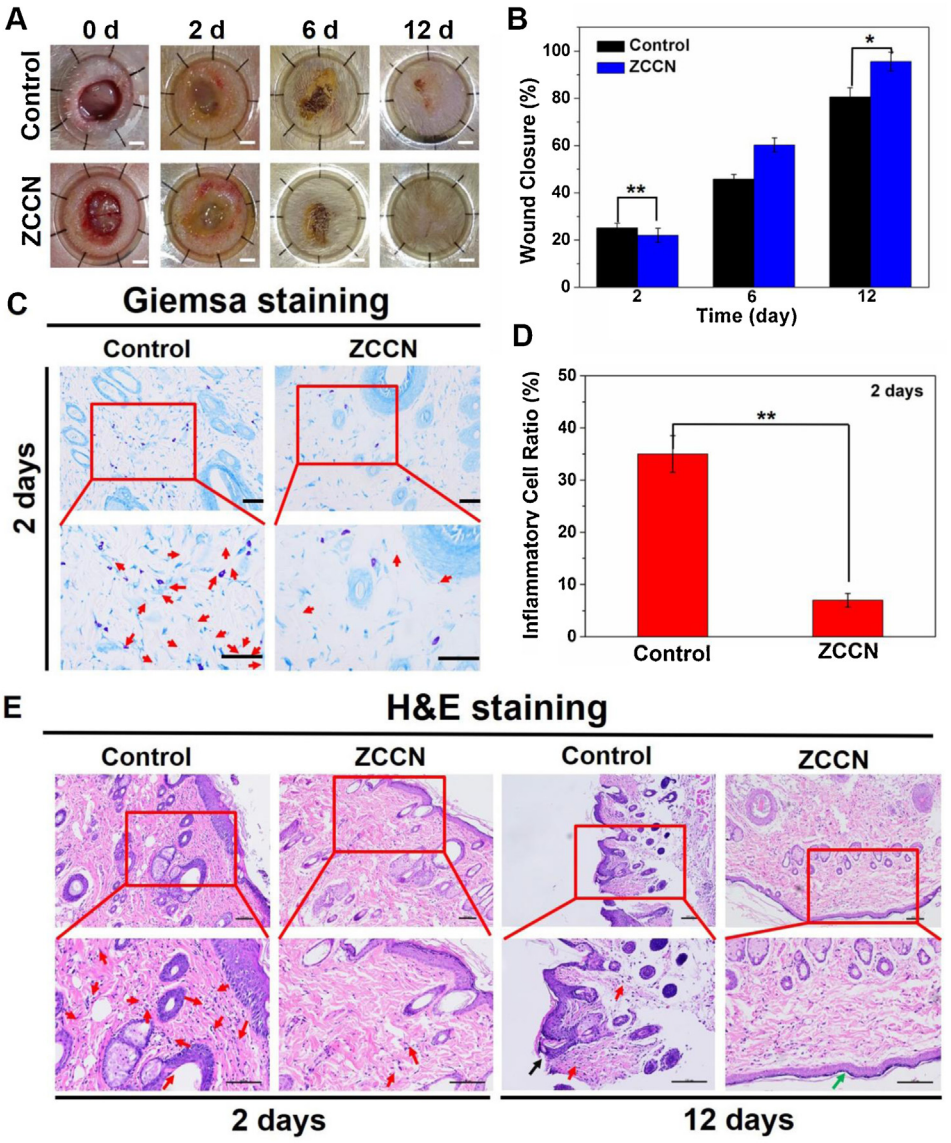

Fig. 7. *in vivo* assessment of the ZCCN with antibacterial effects and wound healing capability. (A) Photographs of the *S. aureus*-infected wounds treated with different dressings at time points of 0, 2, 6 and 12 days. Scale bars, 2 mm. (B) Corresponding wound area at the different time points. (C) Giemsa stained images showing the degree of infection in the wound area after a 2-day treatment. Scale bars are 50 μm. (D) Inflammatory cell ratios calculated from H&E staining data. Inflammatory cell ratios = [(total area of lymphocyte, monocytes, and neutrophil)/area of tissue] × 100 %. (E) H&E stained images showing the degree of infection of the skin tissue after 2 and 12 days. Scale bars are 50 μm. The error bars indicate means ± standard deviations: $^{*}p < 0.05$, $^{**}p < 0.01$.

the 7-day stage. This evidence proved that the cell viability of all the experimental groups was much higher than that of the negative groups, indicating that CCN and ZCCN had excellent cytocompatibility. To explore the effects of light on cells, the cell viability with and without 15 min visible light irradiation at 1-day stage was shown in Fig. 6(B). It was obvious that the cell viability of the light groups did not decrease much compared to the dark groups. The cell viabilities of all the experimental groups were greater than 80 %, revealing that light irradiation had no adverse effect on the cells in this work.

The expression levels of genes (MMP-2, COL-I, and COL-III) involved in tissue repair were analyzed by a quantitative real-time polymerase chain reaction (qRT-PCR). Generally, the MMP-2 gene provides instructions for making a polypeptide that depends on Zn^{2+}, and this polypeptide could eventually become part of the extracellular matrix [48]. After 2 and 5 days, the MMP-2 level of ZCCN group was significantly higher than the control and CCN groups (Fig. 6(C)) due to the large amount of Zn^{2+} released from the ZCCN (Fig. S4 in Supporting Information). At the same time, the expression levels of COL-I (Fig. 6(D)) and COL-III (Fig. 6(E)) also increased with culturing time. In general, the COL-I and COL-III are beneficial for extracellular matrix regeneration and wound repair. These results suggested that ZCCN had excellent effect on accelerating wound repair, ascribing to the function of release Zn^{2+} [49].

3.5. *In vivo* wound healing test

The animal experiment was prepared by rats, and the wounds (5 mm diameters) were infected with 20 μL of *S. aureus* (1×10^8 CFU/mL) to evaluate the wound healing ability of ZCCN (with a PBS control group). As shown in Fig. 7(A), photos of the wounds were recorded on day 0, 2, 6, and 12. All the wounds showed severe infection by *S. aureus* with ichor on day 2. On day 6, the

sizes of all wounds became smaller both in the control group and the experimental group, the latter reaching a smaller size. On day 12, the experimental group almost achieved complete recovery, while the control group showed clear trauma. The changes of the wound closure are shown in Fig. 7(B), revealing that the experimental group achieved an accelerated speed to recover better than the control group. The Giemsa stained wounds on day 2 are shown in Fig. 7(C). There were obvious viable bacteria (red arrows in the high magnification images) in the wound tissues. In contrast, the group treated with ZCCN had far less bacteria than the other groups, due to the impressive antibacterial effect of ZCCN irradiated under 15 min visible light. The hematoxylin and eosin (H&E) were performed to stain wound tissues and the inflammatory cell ratio was calculated from H&E staining images. As shown in Fig. 7(D) and (E). Many inflammatory cells (GRAN, neutrophil granulocyte, red arrows) were observed in the control groups after 2 days. At the 12-day stage, necrosis of epidermal cells and epidermal clefts (black arrows) were also observed in the control group. In contrast, a small number of inflammatory cells were found in the wounds irradiated under visible light in the ZCCN groups. After 12 days, the ZCCN group with light treatment showed the regeneration healing effect, and intact subcutaneous tissue structure (green arrows) were observed.

Moreover, as illustrated in Fig. S5 (in Supporting Information), the toxicity of the samples *in vivo* was tested by routine blood analysis, including white blood cells (WBC), GRAN, red blood cells (RBC), platelets (PLT), hemoglobin (HGB), and hematocrits (HCT). All parameters tested in the experimental group were in the normal level. Furthermore, Fig. S6 (in Supporting Information) showed the historical analysis of the major organs (heart, liver, spleen, lungs, kidney) of the rats after 12 days of treatment, and no abnormal symptoms or damage were observed, proving that the samples were safe for normal tissues *in vivo* during wound healing.

4. Conclusion

In summary, a Z-scheme heterojunction of ZnO-CDots-C_3N_4 for photoresponsive bacteria-killing and acceleration of wound healing system was successfully constructed by a simple method. The CDots allowed the photoinduced electrons to transfer from the CB of ZnO to the VB of g-C_3N_4. Characterization results showed that this system produced a large number of ROS and heat which endowed ZCCN with excellent photoresponsive antibacterial activity by rapidly generating ROS and hyperthermia under visible light irradiation. In addition, the Zn^{2+} released from the ZCCN could intrude into bacterial membrane and promote the proliferation of fibroblasts, thus providing a long-lasting antibacterial property and wound healing property. Our results showed that ZCCN had a great potential for the repairing the damaged skin tissues with bacterial infection.

Acknowledgements

This work is supported by the National Key R&D Program of China (No. 2016YFC1100600 and sub-project No. 2016YFC1100604), the National Science Fund for Distinguished Young Scholars (No. 51925104), the National Natural Science Foundation of China (Nos. 51671081 and 51871162), the Natural Science Fund of Hubei Province (No. 2018CFA064), and Hong Kong ITC (Nos. ITS/287/17 and GHX/002/14SZ), Health and Medical Research Fund (No. 03142446), as well as Hong Kong RGC GRF (No. 17214516) and RGC/NSFC (No. N_HKU725-16).

Appendix A. Supplementary data

Supplementary material related to this article can be found, in the online version, at doi:https://doi.org/10.1016/j.jmst.2020.05.016.

References

[1] R. Wang, T.P. Lai, P. Gao, H. Zhang, P.L. Ho, P.C.Y. Woo, G. Ma, R.Y.T. Kao, H.Y. Li, H.Z. Sun, Nat. Commun. 9 (2018) 439.
[2] C. Dhand, M. Venkatesh, V.A. Barathi, S. Harini, S. Bairagi, E.G.T. Leng, N. Muruganandham, K.Z.W. Low, M.H.U.T. Fazil, X.J. Loh, Biomaterials 138 (2017) 153–168.
[3] C.M. Courtney, S.M. Goodman, T.A. Nagy, M. Levy, P. Bhusal, N.E. Madinger, C.S. Detweiler, P. Nagpal, A. Chatterjee,Sci. Adv. 3 (2017), e1701776.
[4] H. Johnoston, G. Hutchion, F. Christensen, Crit. Rev. Toxicol. 40 (2010) 328–346.
[5] E.L. Zhang, S. Fu, R.X. Wang, H.X. Li, Y. Liu, Z.Q. Ma, G.K. Liu, C.S. Zhu, G.W. Qin, D.F. Chen, Rare Met. 38 (2019) 476–494.
[6] Y. Li, X.M. Liu, L. Tan, Z.D. Cui, X.J. Yang, Y.F. Zheng, K.W.K. Yeung, P.K. Chu, S.L. Wu,Adv. Funct. Mater. 28 (2018), 1800299.
[7] G.Y. Liu, J.H. Zou, Q.Y. Tang, X.Y. Yang, Y.W. Zhang, Q. Zhang, W. Huang, P. Chen, J. Shao, X.C. Dong, ACS Appl. Mater. Interfaces 9 (2017) 40077–40086.
[8] L. Tan, J. Li, X.M. Liu, Z.D. Cui, X.J. Yang, S.L. Zhu, Z.Y. Li, X.B. Yuan, Y.F. Zheng, K.W.K. Yeung, H.B. Pan, X.B. Wang, S.L. Wu,Adv. Mater. 30 (2018), 1801808.
[9] R. Kuriki, K. Maeda, Phys. Chem. Chem. Phys. 19 (2017) 4938–4950.
[10] J. Low, B. Cheng, J. Yu, Appl. Surf. Sci. 392 (2017) 658–686.
[11] Y.L. Liu, X. Li, M. Yang, J.P. Zhang, L.N. Lin, X. Zhao, W.X. Hou, C.L. Zhang, Q. Zhang, F. Pan, G. Alfranca, Y.M. Yang, J.M. Fuente, J. Ni, D.X. Cui, Theranostics 7 (2017) 1650–1662.
[12] W.X. Hou, X. Zhao, X.Q. Qian, F. Pan, C.L. Zhang, Y.M. Yang, J.M. Fuente, D.X. Cui, Nanoscale 8 (2016) 104–116.
[13] M. Mousavi, A.H. Yangjeh, D. Seifzadeh, J. Mater. Sci. Technol. 34 (2018) 1638–1651.
[14] S.Q. Zhao, Z.Y. Tang, S.J. Guo, M.M. Han, C. Zhu, Y.J. Zhou, L. Bai, J. Gao, H. Huang, Y.Y. Li, ACS Catal. 8 (2017) 188–197.
[15] X.H. Wu, F.Y. Chen, X.F. Wang, H.G. Yu, App. Surf. Sci. 427 (2018) 645–653.
[16] M.G. Kim, W.K. Jo, J. Mater. Sci. Technol. 40 (2020) 168–175.
[17] X.F. Lu, Q.L. Wang, D.L. Cui, J. Mater. Sci. Technol. 26 (2010) 925–930.
[18] M. Li, L.X. Zhang, X.Q. Fan, Y.J. Zhou, M.Y. Wu, J.L. Shi, J. Mater. Chem. A 3 (2015) 5189–5196.
[19] S.J. Guo, S.Q. Zhao, X.Q. Wu, H. Li, Y.J. Zhou, C. Zhu, N.J. Yang, X. Jiang, J. Gao, L. Bai, Nat. Commun. 8 (2017) 1828.
[20] M. Jourshabani, Z. Shariatinia, A. Badiei, J. Mater. Sci. Technol. 34 (2018) 1511–1525.
[21] J. Liu, Y. Liu, N.Y. Liu, Y.Z. Han, X. Zhang, H. Huang, Y. Lifshitz, S.T. Lee, J. Zhong, Z. Kang, Science 347 (2015) 970–974.
[22] W. Bing, Z.W. Chen, H.J. Sun, P. Shi, N. Gao, J.S. Ren, X.G. Qu, Nano Res. 8 (2015) 1648–1658.
[23] H.G. Yu, F.Y. Chen, F. Chen, X.F. Wang, Appl. Surf. Sci. 358 (2015) 385–392.
[24] D.W. Zheng, B. Li, C.X. Li, J.X. Fan, Q. Lei, C. Li, Z.S. Xu, X.Z. Zhang, ACS Nano 10 (2016) 8715–8722.
[25] F.L. Wang, P. Chen, Y.P. Feng, Z.J. Xie, Y. Liu, Y.H. Su, Q.X. Zhang, Y.F. Wang, K. Yao, W.Y. Lv, Appl. Catal. B 207 (2017) 103–113.
[26] H. Yu, H.C. Zhang, H. Huang, Y. Liu, H.T. Li, H. Ming, K.H. Kang, New J. Chem. 36 (2012) 1031–1035.
[27] S.W. Cao, J.X. Low, J.G. Yu, M. Jaroniec, Adv. Mater. 27 (2015) 2150–2176.
[28] P. Zhou, J.G. Yu, M. Jaroniec, Adv. Mater. 26 (2014) 4920–4935.
[29] Y.W. Ren, Y.J. Han, Z.D. Cui, X.M. Liu, Z.Y. Li, S.L. Zhu, Y.Q. Liang, S.L. Wu, Bioact. Mater. 5 (2020) 201–209.
[30] H.J. Yu, R. Shi, Y.F. Zhao, G.I. Waterhouse, L.Z. Wu, C.H. Tung, T. Zhang, Adv. Mater. 28 (2016) 9454–9477.
[31] Y.M. Xiang, C.Y. Mao, X.M. Liu, Z.D. Cui, D.D. Jing, X.J. Yang, Y.Q. Liang, Z.Y. Li, S.L. Zhu, Y.F. Zheng, K.W.K. Yeung, D. Zheng, X.B. Wang, S.L. Wu,Small 15 (2019), 1900322.
[32] P.P. Liang, Q.Y. Tang, Y. Cai, G.Y. Liu, W.L. Si, J.J. Shao, W. Huang, Q. Zhang, X.C. Dong, Chem. Sci. 8 (2017) 7457–7463.
[33] B. Huang, L. Tan, X.M. Liu, J. Li, S.L. Wu, Bioact. Mater. 4 (2019) 17–21.
[34] X.H. Wang, K. Su, L. Tan, X.M. Liu, Z.D. Cui, D.D. Jing, X.J. Yang, Y.Q. Liang, Z.Y. Li, S.L. Zhu, K.W.K. Yeung, D. Zheng, S.L. Wu, ACS Appl. Mater. Interfaces 11 (2019) 15014–15027.
[35] L.M. Plum, L. Lothar, H. Haase, Int. J. Environ. Res. 7 (2010) 1342–1365.
[36] J.G. Yu, K. Wang, W. Xiao, B. Cheng, Phys. Chem. Chem. Phys. 16 (2014) 11492–11501.
[37] X.C. Wang, K. Maeda, A. Thomas, K. Takanabe, G. Xin, J.M. Carlsson, K. Domen, M. Antonietti, Nat. Mater. 8 (2009) 76.
[38] K. Wang, Q. Li, B.S. Liu, B. Cheng, W.K. Ho, J.G. Yu, Appl. Catal. B 176 (2015) 44–52.
[39] L.J. Liu, Ceram. Int. 42 (2016) 12516–12520.
[40] W.C. Wan, S. Yu, F. Dong, Q. Zhang, Y. Zhou, J. Mater. Chem. A 4 (2016) 7823–7829.
[41] Y.J. Wang, R. Shi, J. Lin, Y.F. Zhu, Energy Environ. Sci. 4 (2011) 2922–2929.
[42] T.M. Di, B.C. Zhu, B. Cheng, J.G. Yu, J.S. Xu, J. Catal. 352 (2017) 532–541.

[43] C.S. Lei, M. Pi, C.J. Jiang, B. Cheng, J.G. Yu, J. Colloid Interface Sci. 490 (2017) 242–251.
[44] R. Cai, J.G. Wu, L. Sun, Y.J. Liu, T. Fang, S. Zhu, S.Y. Li, Y. Wang, L.F. Guo, C.E. Zhao, Mater. Des. 90 (2016) 839–844.
[45] W.J. Ong, L.L. Tan, Y.H. Ng, S.T. Yong, S.P. Chai, Chem. Rev. 116 (2016) 7159–7329.
[46] C.Y. Mao, Y.M. Xiang, X.M. Liu, Z.D. Cui, X.J. Yang, K.W.K. Yeung, H.B. Pan, X.B. Wang, P.K. Chu, S.L. Wu, ACS Nano 11 (2017) 9010–9021.
[47] J.M. Zhang, Y.H. Sun, Y. Zhao, Y.L. Liu, X.H. Yao, B. Tang, R.Q. Hang, Rare Met. 38 (2019) 552–560.
[48] R.D. Brown, G.M. Jones, R.E. Laird, P. Hudson, C.S. Long, Biochem. Biophys. Res. Commun. 362 (2007) 200–205.
[49] A.B. Lansdown, U. Mirastschijski, N. Stubbs, E. Scanlon, M.S. Agren, Wound Repair Regen. 15 (2007) 2–16.